ACS NANO

www.acsnano.org

ARTICLE

Light-Triggered Droplet Gating Strategy Based on Janus Membrane Fabricated by Femtosecond Laser

Kangru Cheng,[§] Wenlong Xu,[§] Hao Wu,* Bowen Chen, Haoxiang Yang, Zehang Cui, Hao Yu, Zilong Cheng, Yanlei Hu, Jiawen Li, Hongyuan Jiang, Jiaru Chu, and Dong Wu*

Cite This: https://doi.org/10.1021/acsnano.4c08108

Read Online

ACCESS | Metrics & More | Article Recommendations | Supporting Information

ABSTRACT: The characteristics of the directed transport of liquids based on Janus membranes play a crucial role in practical applications in energy, materials, physics, chemistry, medicine, biology, and other fields. Although extensive progress has been made, it is still difficult to realize the accurate controllability of liquid directional transmembrane transport. The current gating strategies for the directed transport of liquids based on Janus membranes still have some limitations: (a) using magnetic fluid may cause contamination due to the addition of new substances and (b) utilizing hydrophobicity/hydrophilicity conversion of titanium dioxide requires a long switching time (over 30 min). Herein, a strategy is proposed to precisely control liquid directional transport by altering the wettability of droplets on Janus films prepared by a femtosecond laser through photothermal effects. Infrared laser irradiation on Janus film coated with CNTs can effectively convert light energy into thermal energy, rapidly increase the surface temperature of Janus film, and change the wettability of the liquid on the film. Liquid transmembrane directional transport can be achieved within a few seconds without contaminating the transported liquid. The proposed gating strategy can enable the application of Janus membranes in various scenarios such as microchemical reactions, biological cell culture, and interface self-propulsion.

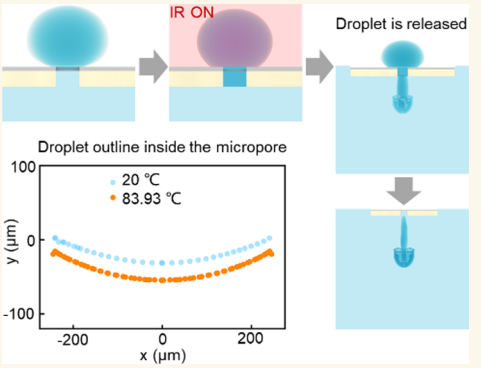

KEYWORDS: *femtosecond laser, wettability, droplet transport, Janus membranes, light-triggered*

1. INTRODUCTION

The directed transport of liquids holds broad applications, such as fog collection,[1−6] chemical microreactions,[7−10] biomedical diagnostics, and so on.[11−14] Researchers have successfully achieved directed transport of liquids through various means, among which Janus membrane technology, placing hydrophilic and hydrophobic layers on two sides of the membrane, has become a research hotspot by enabling spontaneous directed transport of liquids via Laplace pressure without the need for external energy input.[15−21] However, due to the spontaneous nature of directed liquid droplet transport facilitated by Janus membrane technology, achieving precise gating control over droplet transport has become a challenge.[22] To address this issue, researchers have proposed several strategies: (a) coating the membrane surface with magnetic fluid and controlling the opening/closing of membrane pores through external magnetic fields to regulate the on/off state of directed liquid transport.[21,23,24] However, this strategy introduces new liquid substances and is prone to contaminating the transported liquid; (b) utilizing the hydrophobicity/hydrophilicity conversion of titanium dioxide under UV irradiation to regulate the on/off state of directed liquid transport.[20,25,26] However, due to the lengthy hydrophobicity/hydrophilicity conversion time of titanium dioxide under UV irradiation (over 30 min), this strategy exhibits poor responsiveness and cannot achieve precise gating control on directed liquid transport. Therefore, there is an urgent need to develop a contamination-free and fast-responsive strategy to achieve precise gating control over liquid droplet transport based on Janus membrane technology.

Herein, we propose a strategy for precise gating control of liquid directional transport by altering the liquid's wettability on the Janus membrane through the photothermal effect. Our

Received: June 18, 2024
Revised: October 29, 2024
Accepted: November 5, 2024

composite membrane is composed of PDMS (polydimethylsiloxane), customized PET (polyethylene terephthalate), and carbon nanotubes (CNTs), and it is named a CNTs-coated light-triggered Janus membrane (CLJM). By irradiating with an infrared laser, the CNTs on the CLJM can efficiently convert light energy into heat energy, rapidly raising the surface temperature of the CLJM.[27−29] The rapid increase in temperature greatly alters the wettability of the liquid on the CLJM, causing the contact line of the liquid droplet to move down. Under the influence of Laplace pressure, the micropore of the CLJM becomes open, completing the gating control of directional liquid transport.[30,31] Due to the efficient photothermal conversion of CNTs and the noncontact nature of the infrared laser, our CLJM achieves gating control of directional liquid transport in just several seconds and does not contaminate the transported liquid. Furthermore, by establishing a theoretical model of the contact line variation of the liquid droplet on the CLJM surface with temperature, the lower outline of the liquid droplet in the CLJM micropore at different temperatures is accurately predicted and verified. Thus, the entire process of gating control for directional liquid transport is clearly demonstrated. Meanwhile, on the basis of our CLJM, applications including microchemical reactions, cell culture, and self-propulsion are developed.

2. RESULTS

2.1. Fabrication of CLJM and Light-Triggered Droplet Release. The fabrication process of CLJM is illustrated schematically in Figure 1a. First, PDMS and PET films are bonded into a composite film after plasma treatment. Then, the surface of the PDMS film is treated with femtosecond laser ablation to induce rough micro-/nanostructures, followed by an even spray of CNTs. In this way, the PET side of the composite membrane exhibits good hydrophilicity, while the treated PDMS surface exhibits superhydrophobicity (Figure S1, Supporting Information). Meanwhile, the PDMS film and PET film can bond well together, and CNTs can also adhere well to the PDMS surface treated by femtosecond laser (Figures S2 and S3, Supporting Information). Finally, femtosecond laser cutting is employed to cut the desired shape of the CLJM. The photo and SEM images (cross-section, top and bottom) of the CLJM (outer diameter: 8 mm, inner diameter: 500 μm) are presented in Figure 1b. The thickness of the upper PDMS layer is 50 μm, while the thickness of the lower PET layer is 250 μm.

The schematic diagrams and real-time images of the application scenario for CLJM are presented in Figure 1c. The CLJM is positioned at the liquid−gas interface. The liquid level within the CLJM's pore rises to the junction between PET and PDMS layers, driven by capillary effects (Figure S4, Supporting Information).[32,33] The droplet (8 μL) placed on the CLJM pore remains ellipsoid due to surface tension and the hydrophobic PDMS layer. When infrared light irradiates the CLJM, CNTs rapidly convert light into heat, thereby raising the CLJM's temperature. The increase in the temperature leads to intensified molecular motion, thereby gradually enhancing the wettability of the droplet on the surface of PDMS sprayed with CNTs. The contact line of the droplet inside the small pores also begins to gradually descend, making contact with the liquid below, thus completing the release of the droplet under the influence of Laplace pressure. As depicted in Figure 1c, approximately 5.94 s after infrared light irradiation on the CLJM, the droplet within the micropore

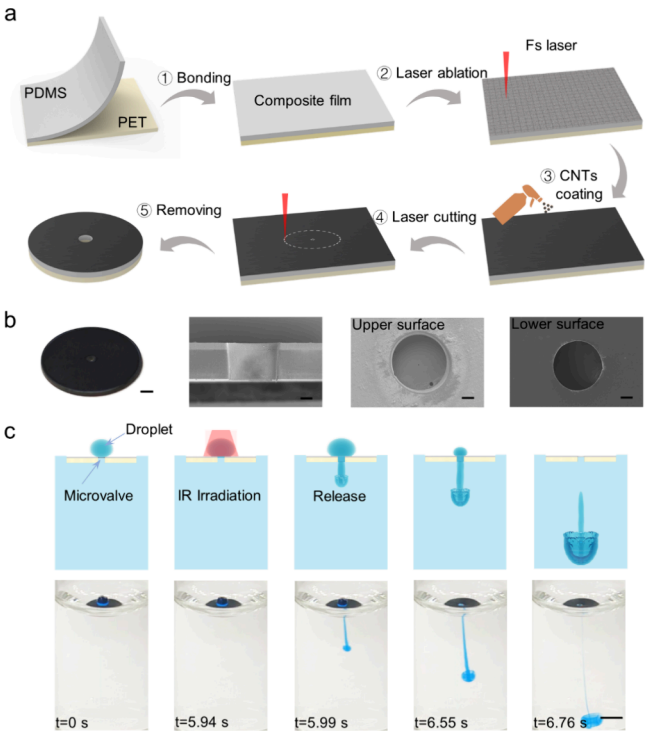

Figure 1. Fabrication of CLJM and the droplet-release process. (a) Manufacturing process of CLJM includes plasma cleaning and bonding of PDMS and PET films, femtosecond laser treatment of PDMS surfaces, and spraying of CNTs. Finally, the CLJM was accurately cut using femtosecond laser. (b) Photo of CLJM, SEM images of micropore cross-section and the upper and lower surfaces. Scale bar for the photo, 1 mm. Scale bar for SEM images, 100 μm. (c) Process of controlled release of the droplet on CLJM under infrared light irradiation. The droplet (8 μL) continuously receiving infrared radiation on the micropore, the contact line of the droplet inside the micropore gradually moves downward and releases after contacting the water surface below. Scale bar, 5 mm.

makes contact with the liquid surface, initiating release under Laplace pressure difference, forming a mushroom-shaped jet (Video S1, Supporting Information). Therefore, through infrared light illumination, controllable release of droplets is achieved, and CLJM functions as a light-trigged valve. Furthermore, not just droplets, our CLJM enables light-triggered gating control of large volumes of liquids (e.g., 300 μL) in the pipeline (Figure S5, Supporting Information). Extreme environment testing and robustness testing have also demonstrated the stability of CLJM and the potential of our strategy (Figures S6 and S7, Supporting Information).

2.2. Mechanism of Light-Triggered Droplet Release on CLJM. In Figure 2a, an initial 8 μL droplet was placed on the CLJM, maintaining superhydrophobicity with an initial contact angle of approximately 157.0°. Upon activation of the infrared light to irradiate the CLJM, CNTs absorb heat, and the temperature of the CLJM gradually increases with increasing irradiation time. As the temperature increases, molecular thermal motion intensifies, leading to the gradual wetting of the surface of CLJM by the droplet. Within 10.0 s, the contact angle gradually decreased to around 139.8° (Video S2, Supporting Information). Figure 2b illustrates a simulation diagram depicting the variation of the lower contour curve of the droplet at different temperatures (from 20 to 83.93 °C). For a 500 μm diameter micropore and an 8 μL droplet size, the

https://doi.org/10.1021/acsnano.4c08108
ACS Nano XXXX, XXX, XXX−XXX

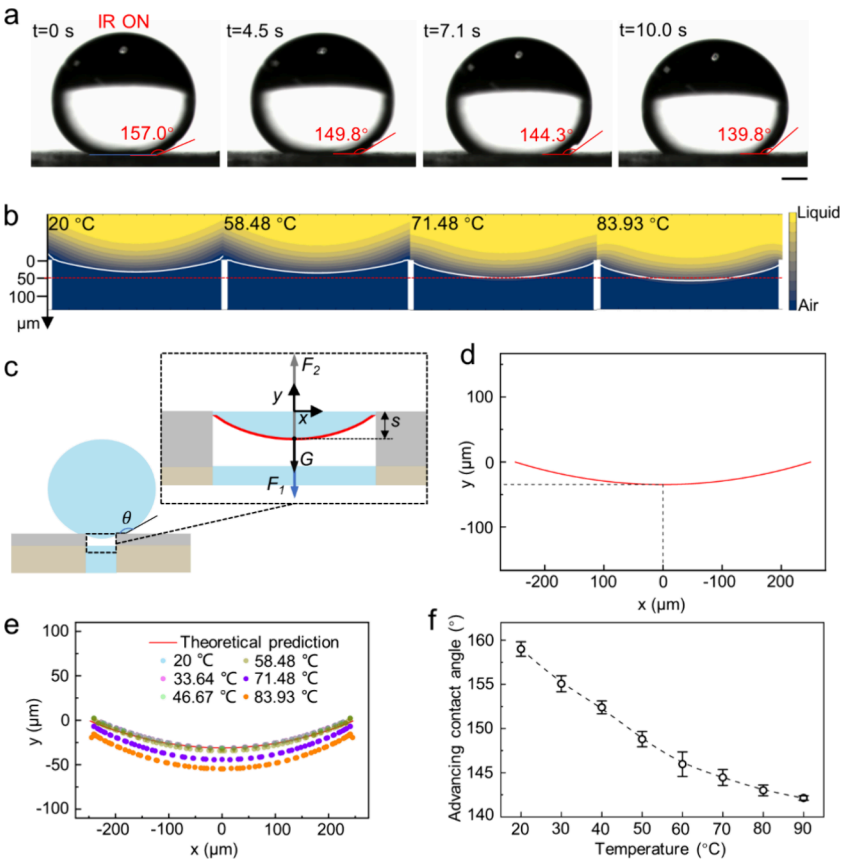

Figure 2. Mechanism of light-triggered droplet release on the CLJM. (a) As the infrared light continues to irradiate, the droplet gradually wets the surface of PDMS coated with CNTs, and the contact angle gradually increases from an initial 157.0° to 139.8°. Scale bar, 500 μm. (b) Simulation diagram of the lower contour curve of the droplet at different temperatures. As the temperature of CLJM gradually increases, the lower contour curve of the droplet gradually moves down. (c) Model image indicates the contact angle (θ), Laplace pressure of the lower surface (F2), Laplace pressure of the upper surface (F1), gravity (G), and the distance (S) between the lowest point of the droplet and the PDMS surface. The x−y coordinate system is established at the center. (d) In the scenario of a micropore diameter (500 μm), a droplet (8 μL), a contact angle (157.0°), and a surface tension (72.8 mN m^{-1}), the shape of the theoretical curve of the lower edge of the droplet cross-section in the micropore was obtained by solving using MATLAB. (e) In the scenario of a micropore diameter (500 μm), a droplet (8 μL), a contact angle (157.0°), and a surface tension (72.8 mN m^{-1}), the outline curve diagram of the droplet at different temperatures. (f) Advancing contact angle data of the PDMS surface treated with femtosecond laser at different temperatures. As the temperature increases, the advancing contact angle gradually decreases.

simulation results indicate that as the wetting of the droplet on the CLJM increases, the contour profile of the droplet gradually shifts downward. The lowest point of the droplet contour line changes gradually from its initial state of 31 to 55 μm.

In order to analyze the process of droplet movement more clearly, the 2D model in Figure 2c is established. The contact angle of the droplet is denoted by θ. The red curve represents the contour curve of the droplet. The distance between the lowest point of the droplet's contour and the upper surface of the CLJM is defined as S. To analyze the forces acting on the lower contour curve of the droplet, we establish an $x-y$ coordinate system, as shown in the figure. Taking any surface element Δs on the contour curve as an example, the surface element is initially subjected to the gravity of the droplet itself, denoted as G:

$$G = \rho g(h - y)\Delta s \tag{1}$$

Among these parameters, ρ represents the density of the droplet. Considering the small volume of the droplet, it can be approximated as a spherical crown. The height (h) of the droplet can be expressed as

$$h = R - R\cos\theta \tag{2}$$

Among these parameters, R denotes the radius of the spherical crown, and v represents the volume of the droplet. The relationship between the radius of the spherical crown and the volume and contact angle of the droplet can be expressed as[30]

$$R = \left[\frac{3v}{\pi(2 - 3\cos\theta + \cos^3\theta)}\right]^{1/3} \tag{3}$$

Next, the contour surface element is subjected to a bending force (F_1) from the surface above the droplet[34,35]:

$$F_1 = \gamma\left(\frac{1}{R} + \frac{1}{R}\right)\Delta s \tag{4}$$

Among these parameters, γ represents the surface tension of the droplet. Third, the contour elements will be subjected to a curvature force (F_2) from the surface below the droplet:

$$F_2 = \gamma\left(\frac{1}{R_1} + \frac{1}{R_2}\right)\Delta s \tag{5}$$

https://doi.org/10.1021/acsnano.4c08108
ACS Nano XXXX, XXX, XXX−XXX

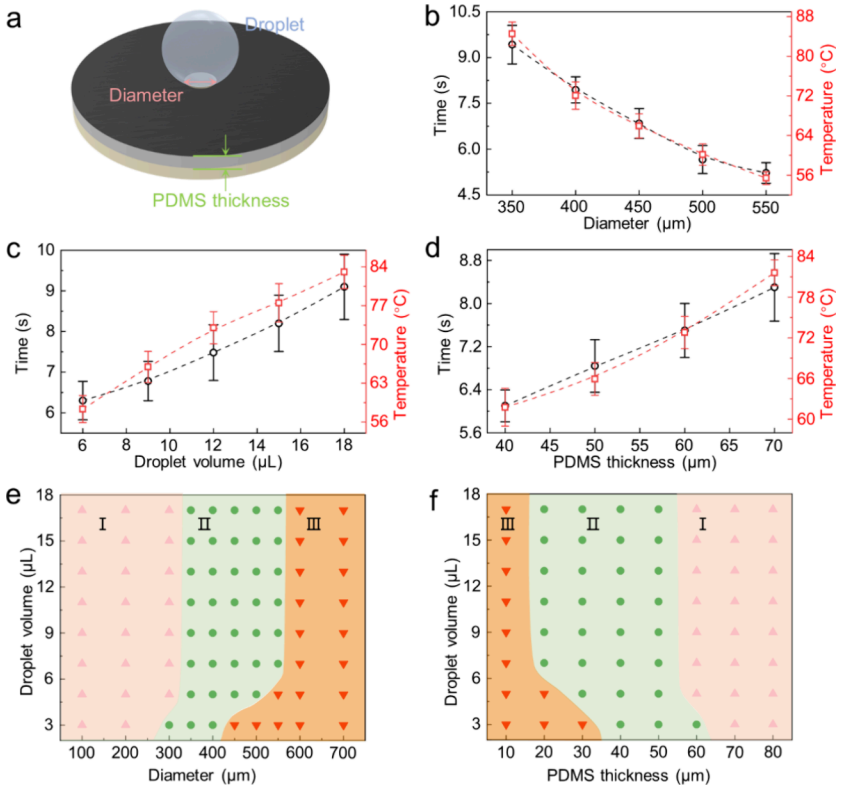

Figure 3. Influence of droplet size, CLJM parameters, and temperature on light-triggered droplet release. (a) Schematic representation of droplet release. Essential parameters influencing the microvalve effect include the droplet volume, micropore diameter, and PDMS thickness. (b) Time and temperature required for the droplet (8 μL) release vary depending on the pore diameter. Within the range of pore diameter from 350 to 550 μm, as the pore diameter increases, the required release time decreases and the temperature decreases (PDMS film thickness: 50 μm). (c) Influence of droplet volume on release time and temperature with a micropore diameter of 450 μm and a PDMS film thickness of 50 μm. Within the range of droplet volumes from 6 to 18 μL, an increase in droplet volume leads to an increase in required release time and temperature. (d) Impact of PDMS membrane thickness on release time and temperature for a droplet (8 μL) with a micropore diameter of 450 μm. The relationship within the PDMS membrane thickness range of 40−70 μm indicates an increase in required release time and temperature as the PDMS membrane thickness increases. (e, f) When the thickness of the PDMS membrane reaches 50 μm or when the pore diameter measures 350 μm, region I represents the scenario where, even under infrared radiation, droplets cannot be released due to the pore diameter being too small or the PDMS membrane being too thick. On the other hand, region III signifies that due to the PDMS membrane being too thin or the pore diameter being too large, droplets cannot be stably placed on the CLJM even without infrared irradiation.

Among these parameters, $1/R_1$ and $1/R_2$ represent the orthogonal curvature of any point on the contour curve of the droplet. This can be expressed as (Figure S8, Supporting Information)[36,37] :

$$\frac{1}{R_1} + \frac{1}{R_2} = \frac{y''}{(1+y'^2)^{3/2}} + \frac{y'}{x\sqrt{1+y'^2}} \tag{6}$$

Considering force balance:

$$F_2 = F_1 + G \tag{7}$$

The obtained contour curve of the droplet satisfies the following differential equation:

$$y'' + \frac{y'}{x}(1+y'^2) - (1+y'^2)^{3/2}\left[\left(\frac{2}{R}\right) + \frac{\rho g}{\gamma}(h-y)\right] = 0 \tag{8}$$

The differential equation satisfied by the contour curve of the droplet reveals that the droplet's shape is primarily influenced by the diameter of the micropore, the volume size of the droplet, surface tension, and contact angle. Utilizing the MATLAB tool and numerical methods, we solve this differential equation, and the resulting contour curve of the droplet is depicted in Figure 2d. The calculated result shows that the value of S is 31 μm. To validate the accuracy of the calculation results, we introduce silicon dioxide fluorescent beads into the droplet and measure the lower contour curve using a confocal microscope. The measurement results indicated that the value of S is 34 μm, which is matched well with the calculation results (Figure S9 and Video S3, Supporting Information). The lower contour curve of the initial state droplet determines whether the droplet can hover on the CLJM rather than directly contact the liquid surface below and cause release. Another crucial factor is the change in the wettability of the droplet on the CLJM caused by continuous infrared irradiation on the CLJM surface sprayed with CNTs. As the droplet gradually spreads out on the surface, the lower contour curve of the droplet also gradually shifts downward. The simulation data is shown in Figure 2e, illustrating the gradual downward movement of the lower contour curve as the temperature increases. To demonstrate changes in wettability, we measured the advancing contact angle data of PDMS surfaces and the contact angle data of the CNTs-sprayed surface at different temperatures (Figure S10,

https://doi.org/10.1021/acsnano.4c08108
ACS Nano XXXX, XXX, XXX−XXX

Supporting Information). The data from Figure 2f of the PDMS surface indicates that as the temperature increases, the advancing contact angle of the droplet gradually decreases. The contour profile of the droplet within the pore will gradually shift downward, thus making contact with the underlying liquid surface and releasing.

2.3. Influence of Droplet Size, CLJM Parameters, and Temperature on Light-Triggered Droplet Release. The ability of the controlled droplet to hover on the CLJM and complete release under infrared light irradiation is determined by factors such as the droplet size, pore diameter, and PDMS film thickness (Figure 3a). When the diameter of the micropore remains constant, an increase in droplet volume results in a decrease in droplet curvature and a reduction in the value of S (the distance between the lowest point of the droplet and the PDMS surface). Conversely, when the droplet size remains constant, the value of S rapidly increases as the diameter of the micropore expands (Figure S11, Supporting Information). Maintaining a constant PDMS film thickness and droplet size, Figure 3b illustrates the time and temperature data for droplet release from CLJM with different apertures under infrared light irradiation. With a fixed PDMS film thickness of 50 μm and a droplet size of 8 μL, as the diameter of the micropore changes from 350 to 550 μm, the droplet's contour line gradually approaches the liquid surface. The infrared irradiation time required for droplet release falls within the range of 9.42−5.22 s, and the corresponding temperature range is 84.54−55.40 °C. Figure 3c, with a fixed PDMS film thickness of 50 μm and a micropore diameter of 450 μm, presents the time and temperature required for the release of different volumes of droplets. As the droplet volume increases from 6 to 18 μL, the droplet curvature decreases, and the initial lower contour line gradually moves away from the liquid surface. The release time spans from 6.30 to 9.10 s, and the temperature ranges from 58.34 to 83.08 °C. In Figure 3d, with a micropore diameter of 450 μm, the relationship between the time required to release an 8 μL droplet and the PDMS film thickness is demonstrated. As the PDMS film thickness increases from 40 to 70 μm, the initial lower contour line of the droplet progressively moves away from the liquid surface. The required release time varies from 6.10 to 8.30 s, and the temperature ranges from 61.76 to 81.60 °C. Evidently, within a certain range, increasing the droplet volume, reducing the micropore diameter, or increasing the PDMS hydrophobic layer thickness will result in an increased infrared heating time required for droplet release, accompanied by an increase in the required temperature.

The effective light-triggered droplet release on the CLJM corresponds to the droplet volume range, pore diameter, and PDMS film thickness, as shown in Figure 3e,f. With the PDMS film thickness fixed at 50 μm, Figure 3e presents the phase diagram indicating whether droplets of different volumes under different pore diameters can be released under infrared irradiation. Region II represents the area where droplets can be released through infrared heating on the CLJM. Region I indicates that due to the small diameter of the micropore, the droplet's contour line is far from the liquid surface, making it impossible to alter the droplet's wettability to release it through infrared light irradiation. Region III represents the area where the lower contour line of the droplet is released directly from contact with the liquid surface below without infrared irradiation due to the large diameter of the micropore. The portion of region II can be observed to shift leftward as it approaches the lower part. This shift is due to the contour line of the droplet moving away from the liquid surface, compensated for by the downward movement caused by the larger curvature of the smaller droplet. When the diameter of the micropore is fixed at 350 μm, Figure 3f illustrates the phase diagram indicating whether droplets of different volumes can be released under infrared radiation with different PDMS film thicknesses. Region I indicates that due to the thick PDMS film, the contour curve of the droplet is far away from the liquid surface, making it unable to be released through infrared irradiation. Region III indicates that due to the thin PDMS film, the droplet cannot be placed on CLJM and is released directly. The area II that satisfies the infrared light-controlled release of the droplet is seen to shift rightward at the bottom of the phase diagram. This shift occurs because the larger curvature of the smaller droplet compensates for the influence of the thicker hydrophobic film on the droplet's lower contour line, which would otherwise be farther away from the liquid surface.

2.4. Applications of the CLJM in Microchemical Reactions and Microbial Culture. Our strategy for light-triggered droplet release on the CLJM has potential applications in the fields of microchemical reactions, microbiology, and cell culture. In microchemical reactions, where many toxic experiments often require conduction in closed containers with noncontact operations, stringent demands are placed on experimental methods and environments. Our strategy of light-triggered droplet release on the CLJM presents promising applications in the microchemical reactions field. Figure 4a illustrates the microchemical reaction test chamber, where the CLJM is suspended in the solution and different reaction droplets are placed on the micropores of the CLJM. An external infrared light source is used to control the release of specific droplets as needed. We have designed an experimental setup and demonstration of microchemical reactions, as depicted in Figure 4b. Two micropores are fabricated on a CLJM (Figure S12, Supporting Information). The CLJM is placed on top of a 0.01 mol L^{-1} silver nitrate solution, with 6 μL of 0.5 mol L^{-1} sodium chloride solution and 0.1 mol L^{-1} sodium sulfide solution on the two micropores, respectively. The setup is enclosed with a glass slide to simulate a closed experimental environment. Initially, the sodium chloride droplet was irradiated with infrared light, and after 4.49 s, the droplet was released into the silver nitrate solution, resulting in the formation of a white precipitate of silver chloride. After the reaction stabilized, the sodium sulfide droplet was irradiated with infrared light. Approximately 6.75 s later, the droplet was released into the silver nitrate solution, initiating a reaction that produced a black precipitate of silver sulfide (Video S4, Supporting Information). Our strategy also has excellent universality for droplets with various chemical properties (Figure S13, Supporting Information). At the same time, the sequential release of droplets demonstrates the flexibility and controllability of our strategy.

Our strategy also holds promising applications in the fields of cell culture and microbiology. In the process of culturing cells using a live cell workstation, there is often a need to deliver different drugs to cells to adjust their survival status in response to various cell states. Specifically, during the cultivation of Hela cells on a live cell workstation, we employed the CLJM to release varying amounts of DOX drugs, enabling the continuous observation of the cell survival status. Staining the cells with trypan blue at regular intervals

https://doi.org/10.1021/acsnano.4c08108
ACS Nano XXXX, XXX, XXX−XXX

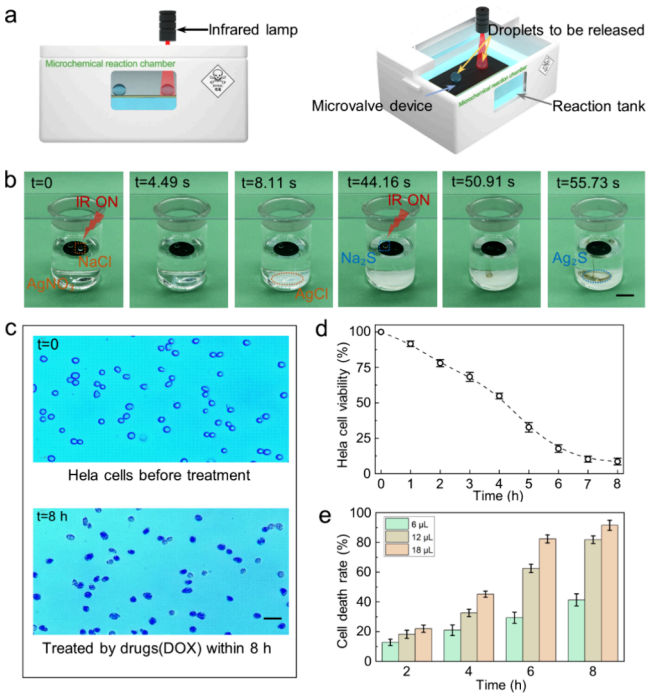

Figure 4. Application of the CLJM in the field of microchemical reactions and microbial culture. (a) Light-triggered microchemical reaction experimental box consists of a box body, an external infrared light source, CLJM, droplets to be reacted, a reaction environment, etc. (b) Sodium chloride droplet and the sodium sulfide droplet are sequentially released by light control and react with the silver nitrate solution. Scale bar, 10 mm. (c, d) While cultivating Hela cells on a live cell workstation, 18 μL of DOX drugs at a concentration of 5 mg mL^{-1} were released through a light-controlled method. The cultivation lasted for 8 h, and subsequently, trypan blue staining was used to observe the cell viability. During an 8 h incubation period, the survival rate of Hela cells decreased from 100% to approximately 5%. Scale bar, 50 μm. (e) When cultivating Hela cells in a live cell workstation, cell viability was observed after adding 6, 12, and 18 μL of DOX drugs at a concentration of 5 mg mL^{-1} for sequential cultivation durations of 2−8 h. As the amount of the drugs increased and the cultivation time was extended, the cell survival rate decreased.

allowed us to distinguish inactive cells, which lose membrane selectivity and are stained by trypan blue molecules, from surviving cells, which maintain a round state and remain unstained by trypan blue. Figure 4c shows cell staining images before and 8 h after the release of DOX drugs during the cell culture process. It is evident from the figure that the survival rate of cells before drug release is close to 100%, and the cell mortality rate reaches approximately 95% after 8 h of drug release. As the cultivation time extends, the survival rate of cells gradually decreases following DOX drug intervention. During the cultivation of Hela cells, different volumes of DOX drugs with a concentration of 5 mg mL^{-1} were added. The data on the cell survival rate and culture time are presented in Figure 4e. It is observed that the larger the amount of DOX drugs used for the same culture time, the lower the cell survival rate. Similarly, with the same dosage of DOX drugs, the longer the culture time, the lower the cell survival rate.

2.5. Light-Triggered Small Boat Based on the CLJM.

In addition to the aforementioned applications in microchemical reactions and microbial culture, our CLJM can also be used for driving at the liquid−gas interface. The strategy of controlling droplet release with infrared light on the CLJM demonstrates extensive application potential in the field of controlling object motion at the liquid−gas interface. As illustrated in Figure 5a, after the application of CNTs, we shaped the small boat using femtosecond laser cutting, followed by a tilted treatment of micropore to create our photocontrolled small boat. The SEM image in Figure 5b showcases a 45° oblique micropore machined by femtosecond laser on the CLJM. The inclined treatment of the micropore on the small boat directs the mushroom-shaped jet released from the droplet along the inclined channel, providing the boat with a reverse force to propel it forward.[38−40] Figure 5c displays the schematic diagram of the controlled motion of the small boat along with actual experimental footage. Designing and treating the small boat shape based on ballistics, we machined a straight micropore at a 45° angle in the center position (Figure S14, Supporting Information). After being irradiated by infrared light for about 6 s, the droplet (15 μL) with blue dye above the micropore was released along the inclined micropore for about 0.9 s, propelling the small boat forward with a tilted mushroom-shaped jet trailing behind (Video S5, Supporting Information). In Figure 5d, when the diameter of the micropore is 400 μm, the thickness of the PDMS film is 50 μm, the thickness of the PET film is 250 μm, and the droplet size is 15 μL, the average velocity and droplet release time of the small boat during the droplet release period are related to the inclination angle of the micropore. A smaller inclination angle results in a higher average speed of the small boat. As the inclination angle changes from 15° to 75°, the time for droplet release changes relatively little, while the average speed of the small boat gradually decreases from 27.37 to 12.16 mm s^{-1}. When the fixed inclination angle is 45° and other parameters remain consistent, changing the diameter of the micropore is shown in Figure 5e. As the diameter of the micropore increased from 350 to 550 μm, the duration of droplet release gradually decreased from 0.47 to 0.23 s, and the average speed of the small boat slightly decreased.

3. CONCLUSIONS

In order to address existing issues in gating control over droplet transport using Janus membranes (pollution problem by using magnetic fluid and poor responsiveness by using hydrophobicity/hydrophilicity of titanium dioxide under UV irradiation), we propose a different strategy. This strategy employs the photothermal effect to precisely control liquid directional transport by altering the liquid's wettability on the Janus membrane. Our composite membrane (CLJM) is bonded from hydrophobic PDMS film and hydrophilic PET film and covered with a layer of CNTs after femtosecond laser surface treatment. By irradiation with an infrared laser, the CNTs on the CLJM can efficiently convert light energy into heat energy, rapidly raising the surface temperature of the CLJM. The rapid increase in temperature greatly changes the wettability of liquid on CLJM, causing the contact line of the droplet to move and contact the liquid surface. Under the influence of Laplace pressure, the micropores of CLJM open, completing the gating of liquid directional transportation. Theoretical calculation and analysis on the droplet gating strategy are conducted, which are consistent with the measurement results. In addition, we have established a theoretical model of the contact line variation of the droplet on the CLJM surface with the temperature. The lower outline of the droplet in the CLJM micropore at different temperatures

https://doi.org/10.1021/acsnano.4c08108
ACS Nano XXXX, XXX, XXX−XXX

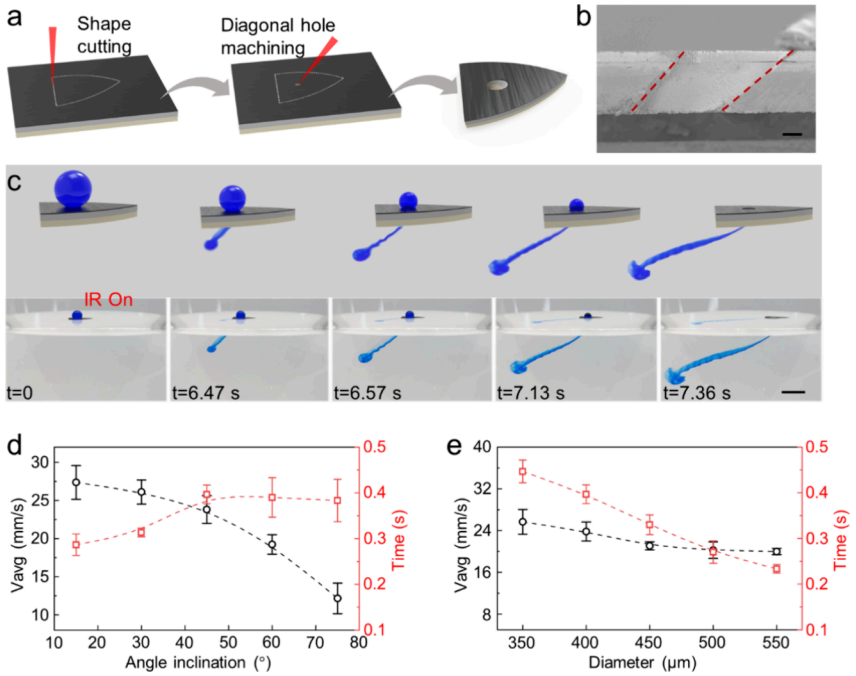

Figure 5. Application of the CLJM in interface drive. (a) Schematic diagrams of cutting the shape of a small boat using a femtosecond laser and then treating the slanted micropore on the boat. (b) SEM image of the cross section of the micropore of the small boat. Scale bar, 100 μm. (c) Duration of the jet at different inclinations and the average velocity of the small boat (PDMS film thickness: 50 μm. Droplet volume: 15 μL. Diameter: 300 μm). Scale bar, 10 mm. (d) Duration and average velocity of the jet from a small boat at different inclinations (PDMS film thickness: 50 μm. Droplet volume: 15 μL. Diameter: 400 μm). (e) Duration and average velocity of small boat spraying at different diameters (PDMS film thickness: 50 μm. Droplet volume: 15 μL. Inclination: 45°).

can be accurately predicted and verified. Based on our CLJM, applications including microchemical reactions, cell culture, and interface boat propulsion have been developed. Our future work will integrate CLJM into microfluidic systems to achieve different devices for better microchemical reactions and biomedical applications. In addition, if the rapid conversion of hydrophobicity/hydrophilicity of composite membranes can be achieved (our current strategy only achieves rapid changes in wettability), then the effect of droplet gating control will be better, which is also a challenge for our future research.

4. EXPERIMENTAL SECTION

4.1. Materials. PDMS and customized PET films were purchased from Taobao, China. CNTs were purchased from Xianfeng Nano (length: 10−30 μm, diameter: 10−20 nm, 100252). The preparation of CNTs solution: add 0.07 g of CNTs to cyclohexane and sonicate for 1.5 h, then add 0.07 g of TPE and sonicate for 1.5 h, and finally add 0.5 mL of Glaco solution. The spray gun was purchased from Taobao (PJR-130, caliber: 0.3 mm). Infrared lasers are produced by Fuzhe Technology Co., Ltd. (FU808AD200-16GD, power: 200 mW, wavelength: 808 nm). The height of the light source from the surface of the sample is 18 cm, and the measured laser power at the sample is 147 mW. FluoSpherestm carboxyl-modified microspheres were purchased from Thermo Fisher (diameter: 1 μm, F8816). The plasma cleaning machine was purchased from ZHONGXINQIHENG company (PDC-MG, MING HENG).

4.2. Femtosecond Laser Fabrication. The femtosecond laser source employed in this work was a Solstice Ace model produced by Spectra-Physics, USA (80L8TICE-ACE-100F-1K). To perform ablation, a laser beam with parameters of 100 fs, 1 kHz, and 800 nm was used, which was focused by an F-theta lens with a focal length of 100 mm. The laser focus was guided using a galvanometer scanner (model: s-9210d) purchased from Sunny Technology, China. Femtosecond laser treatment involved in this project includes orthogonally crossed line-by-line consecutive scanning of the PDMS surface to generate grid micro grooves and laser cutting to generate micropores and shapes. The optimized laser power of 350 mW, scanning speed of 15 mm s^{-1}, and scanning times of 1 were used to treat the PDMS surface. The laser power for cutting the shape and micropore of CLJM is 150 mW; the scanning speed is 2 mm s^{-1}, and the scanning times are 20.

4.3. Characterization. Contact angle measurements were conducted using a CA100C machine (Innuo, China) at ambient temperature. The equipment used for capturing SEM images is a scanning electron microscope (EVO18, ZEISS, Germany). The device used to capture droplet contours is a Leica SP8 confocal laser scanning microscopy (Leica, Germany). The infrared thermal imager was purchased from FOTRIC (FOTRIC322Q, China).

4.4. Simulation Method. The contact infiltration problem of multiphase fluid is mainly controlled by the laminar equation, where the treatment of the liquid−gas interface is completed by the phase field method. The originally sharp interfaces are expressed by a continuous phase-field scalar. In addition, the temperature field is introduced to describe the liquid−gas contact angle that varies with the temperature. The initial temperature is set at 20 °C, and the simulation domain is ultimately heated to 85 °C. A two-dimensional numerical model that satisfies the axisymmetric assumption is established, whose total size of the simulation domain is set to a radius of R = 10 mm and a height of H = 5 mm. Regarding the numerical discretization strategy, unstructured second-order triangular units are utilized within the inner domain, while the structured quadrilateral mesh is employed on the boundary layer of the multiphase contact interface. The intrinsic interface thickness of the phase field is maintained within a range well below the size of the droplet to ensure the conservation of quality and accurate depiction of surface tension. For the time iteration strategy, the generalized α method is employed to ensure model convergence. In the simulation of multiphase laminar flow coupled with temperature fields, the trajectory of the liquid−gas interface, as well as the distributions of fluid pressure and temperature fields, are measured.

https://doi.org/10.1021/acsnano.4c08108
ACS Nano XXXX, XXX, XXX−XXX

ASSOCIATED CONTENT

Supporting Information

The Supporting Information is available free of charge at https://pubs.acs.org/doi/10.1021/acsnano.4c08108.

Process of releasing the droplet on CLJM (MP4)

Change process of contact angle of the droplet on CLJM under continuous infrared light irradiation (MP4)

Process of capturing the contour of the droplet inside micropore using confocal microscope (MP4)

Microchemical reaction demonstration (MP4)

Contact angles of TPU, PVC, and PC films; surface SEM image of PDMS treated with femtosecond laser; comparison of bonding effect between PDMS film and PET film before and after plasma cleaning; model diagram of the CLJM on liquid−gas interface; schematic diagram of liquid release inside the pipeline on CLJM under infrared light irradiation; comparison chart of CLJM before and after 48 h of placement in hydrochloric acid solution and sodium hydroxide solution; robustness test results; establishing the $x-y-z$ three-dimensional coordinate system; measurement of the lower curve profile of the droplet doped with silica fluorescent microspheres with a diameter of 1 μm using confocal microscopy; images of PDMS surface sprayed with CNTs at 20 and 90 °C; theoretical value of the distance between the lowest point of the droplet and the PDMS surface related to the size of the device's aperture and the size of the droplet; design and fabrication diagrams and models of the CLJM for microchemical reactions; contact angles of glycerol aqueous solutions with different volume ratios; and shape design and machining diagram of the small boat (PDF)

Interface self-propulsion demonstration (MP4)

AUTHOR INFORMATION

Corresponding Authors

Hao Wu − *CAS Key Laboratory of Mechanical Behavior and Design of Materials, Key Laboratory of Precision Scientific Instrumentation of Anhui Higher Education Institutes, Department of Precision Machinery and Precision Instrumentation, University of Science and Technology of China, Hefei, Anhui 230027, China*; Email: walech@ustc.edu.cn

Dong Wu − *CAS Key Laboratory of Mechanical Behavior and Design of Materials, Key Laboratory of Precision Scientific Instrumentation of Anhui Higher Education Institutes, Department of Precision Machinery and Precision Instrumentation, University of Science and Technology of China, Hefei, Anhui 230027, China*; orcid.org/0000-0003-0623-1515; Email: dongwu@ustc.edu.cn

Authors

Kangru Cheng − *CAS Key Laboratory of Mechanical Behavior and Design of Materials, Key Laboratory of Precision Scientific Instrumentation of Anhui Higher Education Institutes, Department of Precision Machinery and Precision Instrumentation, University of Science and Technology of China, Hefei, Anhui 230027, China*

Wenlong Xu − *CAS Key Laboratory of Mechanical Behavior and Design of Materials, Department of Modern Mechanics, University of Science and Technology of China, Hefei, Anhui 230027, China*

Bowen Chen − *CAS Key Laboratory of Mechanical Behavior and Design of Materials, Key Laboratory of Precision Scientific Instrumentation of Anhui Higher Education Institutes, Department of Precision Machinery and Precision Instrumentation, University of Science and Technology of China, Hefei, Anhui 230027, China*

Haoxiang Yang − *CAS Key Laboratory of Mechanical Behavior and Design of Materials, Department of Modern Mechanics, University of Science and Technology of China, Hefei, Anhui 230027, China*

Zehang Cui − *CAS Key Laboratory of Mechanical Behavior and Design of Materials, Key Laboratory of Precision Scientific Instrumentation of Anhui Higher Education Institutes, Department of Precision Machinery and Precision Instrumentation, University of Science and Technology of China, Hefei, Anhui 230027, China*

Hao Yu − *CAS Key Laboratory of Mechanical Behavior and Design of Materials, Department of Modern Mechanics, University of Science and Technology of China, Hefei, Anhui 230027, China*

Zilong Cheng − *CAS Key Laboratory of Mechanical Behavior and Design of Materials, Key Laboratory of Precision Scientific Instrumentation of Anhui Higher Education Institutes, Department of Precision Machinery and Precision Instrumentation, University of Science and Technology of China, Hefei, Anhui 230027, China*

Yanlei Hu − *CAS Key Laboratory of Mechanical Behavior and Design of Materials, Key Laboratory of Precision Scientific Instrumentation of Anhui Higher Education Institutes, Department of Precision Machinery and Precision Instrumentation, University of Science and Technology of China, Hefei, Anhui 230027, China*; orcid.org/0000-0003-1964-0043

Jiawen Li − *CAS Key Laboratory of Mechanical Behavior and Design of Materials, Key Laboratory of Precision Scientific Instrumentation of Anhui Higher Education Institutes, Department of Precision Machinery and Precision Instrumentation, University of Science and Technology of China, Hefei, Anhui 230027, China*; orcid.org/0000-0003-3950-6212

Hongyuan Jiang − *CAS Key Laboratory of Mechanical Behavior and Design of Materials, Department of Modern Mechanics, University of Science and Technology of China, Hefei, Anhui 230027, China*; orcid.org/0000-0003-0266-3011

Jiaru Chu − *CAS Key Laboratory of Mechanical Behavior and Design of Materials, Key Laboratory of Precision Scientific Instrumentation of Anhui Higher Education Institutes, Department of Precision Machinery and Precision Instrumentation, University of Science and Technology of China, Hefei, Anhui 230027, China*; orcid.org/0000-0001-6472-8103

Complete contact information is available at: https://pubs.acs.org/10.1021/acsnano.4c08108

Author Contributions

[§]K.C. and W.X. contributed equally to this work.

Notes

The authors declare no competing financial interest.

https://doi.org/10.1021/acsnano.4c08108
ACS Nano XXXX, XXX, XXX−XXX

ACKNOWLEDGMENTS

This work was supported by the National Natural Science Foundation of China (nos. 61927814, 62325507, 62405307, 52122511, U20A20290, 12025207, and 11872357), the National Key Research and Development Program of China (2021YFF0502700), the Anhui Provincial Natural Science Foundation (2308085QF218), China National Postdoctoral Program for Innovative Talents (BX20230351), China Postdoctoral Science Foundation (2023M733382), the Fundamental Research Funds for the Central Universities (WK2090000058), and the Major Scientific and Technological Projects in Anhui Province (202203a05020014). We acknowledge the Experimental Center of Engineering and Material Sciences at USTC for the fabrication and measuring of samples. This work was partly carried out at the USTC Center for Micro and Nanoscale Research and Fabrication.

REFERENCES

(1) Parker, A. R.; Lawrence, C. R. Water capture by a desert beetle. *Nature* **2001**, *414* (6859), 33−34.

(2) Wan, K.; Gou, X. L.; Guo, Z. G. Bio-inspired Fog Harvesting Materials: Basic Research and Bionic Potential Applications. *J. Bionic Eng.* **2021**, *18* (3), 501−533.

(3) Hou, Y. Y.; Gan, Z. H.; Li, H.; Zang, H. X.; Zheng, H. Y.; Lei, H. B.; Liu, M. M.; Yan, C. Y.; Wu, Y. L. Laser-textured biomimetic copper leaf with structural-wettability dual gradient for efficient fog harvesting. *Opt. Laser Technol.* **2024**, *170*, No. 110154.

(4) Zhong, L. S.; Chen, H.; Zhu, L. M.; Zhou, M. L.; Zhang, L.; Yu, D. D.; Wang, S. M.; Han, X. F.; Hou, Y. P.; Zheng, Y. M. Gradient-Janus Wires for Simultaneous Fogwater Harvesting and Electricity Generation. *ACS Nano* **2024**, *18* (14), 10279−10287.

(5) Fu, Y.; Wu, L. S.; Ai, S. L.; Guo, Z. G.; Liu, W. M. Bionic collection system for fog-dew harvesting inspired from desert beetle. *Nano Today* **2023**, *52*, No. 101979.

(6) Yang, H. R.; Zhu, H. J.; Hendrix, M.; Lousberg, N.; de With, G.; Esteves, A. C. C.; Xin, J. H. Temperature-Triggered Collection and Release of Water from Fogs by a Sponge-Like Cotton Fabric. *Adv. Mater.* **2013**, *25* (8), 1150−1154.

(7) Yu, C. S.; Lin, M. Y.; Hu, Y. C.; Fu, T. L.; Chou, H. Y. Self-alignment optical detection system for droplet-based biochemical reactions. In *IEEE Sensors 2004 Conference, Vienna University of Technology, Vienna, Austria, 2004*; IEEE: New York, NY, 2004; pp 1206−1209.

(8) Ji, J.; Zhao, Y. Q.; Guo, L. P.; Liu, B. H.; Ji, C.; Yang, P. Y. Interfacial organic synthesis in a simple droplet-based microfluidic system. *Lab Chip* **2012**, *12* (7), 1373−1377.

(9) Hartman, R. L.; Naber, J. R.; Buchwald, S. L.; Jensen, K. F. Multistep Microchemical Synthesis Enabled by Microfluidic Distillation. *Angew. Chem.-Int. Ed.* **2010**, *49* (5), 899−903.

(10) Jiang, S. J.; Li, B.; Zhao, J.; Wu, D.; Zhang, Y. Y.; Zhao, Z. P.; Zhang, Y. Y.; Yu, H.; Shao, K. X.; Zhang, C.; et al. Magnetic Janus origami robot for cross-scale droplet omni-manipulation. *Nat. Commun.* **2023**, *14* (1), 5455.

(11) Zhang, Y. Y.; Li, J.; Xiang, L.; Wang, J. X.; Wu, T.; Jiao, Y. L.; Jiang, S. J.; Li, C. Z.; Fan, S. Y.; Zhang, J.; et al. A Biocompatible Vibration-Actuated Omni-Droplets Rectifier with Large Volume Range Fabricated by Femtosecond Laser. *Adv. Mater.* **2022**, *34* (12), No. 2108567.

(12) Kumar, D. J. P.; Borkar, C.; Dayal, P. Fast-Moving Self-Propelled Droplets of a Nanocatalyzed Belousov-Zhabotinsky Reaction. *Langmuir* **2021**, *37* (43), 12586−12595.

(13) Shental, N.; Levy, S.; Wuvshet, V.; Skorniakov, S.; Shalem, B.; Ottolenghi, A.; Greenshpan, Y.; Steinberg, R.; Edri, A.; Gillis, R.; et al. Efficient high-throughput SARS-CoV-2 testing to detect asymptomatic carriers. *Sci. Adv.* **2020**, *6* (37), No. eabc5961.

(14) Kevadiya, B. D.; Machhi, J.; Herskovitz, J.; Oleynikov, M. D.; Blomberg, W. R.; Bajwa, N.; Soni, D.; Das, S.; Hasan, M.; Patel, M.; et al. Diagnostics for SARS-CoV-2 infections. *Nat. Mater.* **2021**, *20* (5), 593−605.

(15) Peng, Z. C.; Liu, R. P.; Xu, Z. G.; Chi, H. J.; Wang, Z.; Zhao, Y. Directional sweat transport window based on hydrophobic/hydrophilic Janus fabric enables continuous transfer and monitoring of sweat. *Appl. Mater. Today* **2022**, *29*, No. 101623.

(16) Tian, X. L.; Jin, H.; Sainio, J.; Ras, R. H. A.; Ikkala, O. Droplet and Fluid Gating by Biomimetic Janus Membranes. *Adv. Funct. Mater.* **2014**, *24* (38), 6023−6028.

(17) Zhao, Z. H.; Ning, Y. Z.; Ben, S.; Zhang, X. D.; Li, Q.; Yu, C. M.; Jin, X.; Liu, K. S.; Jiang, L. Liquid-Assisted Single-Layer Janus Membrane for Efficient Unidirectional Liquid Penetration. *Adv. Sci.* **2022**, *9* (2), No. 2103765.

(18) Zhang, J. J.; Liu, H. L.; Jiang, L. Membrane-Based Strategy for Efficient Ionic Liquids/Water Separation Assisted by Superwettability. *Adv. Funct. Mater.* **2017**, *27* (20), No. 1606544.

(19) Deng, W. S.; Wang, G.; Zeng, Z. X.; Ren, T. H. Single-side etching for on-demand and versatile liquid diodes with opposite wettability in multiple systems. *Chem. Eng. J.* **2023**, *452*, No. 138707.

(20) Yu, X. Y.; Kang, S. B.; Jiao, X. Y.; Lai, H.; Wang, R. J.; Cheng, Z. J. A smart underoil″water diode″Janus TiO2 mesh membrane. *Chem. Eng. J.* **2023**, *456*, No. 141038.

(21) Sun, Z. N.; Cao, Z. Y.; Li, Y.; Zhang, Q. Y.; Zhang, X. F.; Qian, J. G.; Jiang, L.; Tian, D. L. Switchable smart porous surface for controllable liquid transportation. *Mater. Horizons* **2022**, *9* (2), 780−790.

(22) Sheng, Z. Z.; Wang, H. L.; Tang, Y. L.; Wang, M.; Huang, L. Z.; Min, L. L.; Meng, H. Q.; Chen, S. Y.; Jiang, L.; Hou, X. Liquid gating elastomeric porous system with dynamically controllable gas/liquid transport. *Sci. Adv.* **2018**, *4* (2), No. eaao6724.

(23) Wang, D. Y.; Zheng, S.; Liu, H.; Tang, J. Y.; Miao, W. N.; Wang, H. T.; Tian, Y.; Yang, H.; Jiang, L. A Magnetic Gated Nanofluidic Based on the Integration of a Superhydrophilic Nanochannels and a Reconfigurable Ferrofluid. *Adv. Mater.* **2019**, *31* (7), No. 1805953.

(24) Cai, J. R.; Zhao, J.; Gao, X. Q.; Ma, W.; Meng, D.; Zhang, H. Y.; Hao, C. L.; Sun, M. Z.; Kuang, H.; Xu, C. L.; Xu, L. G. Magnetic Field Tuning Ionic CurrentGenerated by Chiromagnetic Nanofilms. *ACS Nano* **2022**, *16* (7), 11066−11075.

(25) Yu, X. Y.; Lai, H.; Kang, H. J.; Liu, Y. Y.; Wang, Y. S.; Cheng, Z. J. Underoil Directional Self-Transportation of Water Droplets on a TiO_2-Coated Conical Spine. *ACS Appl. Mater. Interfaces* **2022**, *14* (4), 6274−6282.

(26) Kang, H. J.; Liu, Y. Y.; Lai, H.; Yu, X. Y.; Cheng, Z. J.; Jiang, L. Under-Oil Switchable Superhydrophobicity to Superhydrophilicity Transition on TiO_2 Nanotube Arrays. *ACS Nano* **2018**, *12* (2), 1074−1082.

(27) Joshi, S. R.; Pratap, A.; Kim, S. Ultrathin silk nanofiber-carbon nanotube skin tattoos for wirelessly triggered and temperature feedbacked transdermal drug delivery. *Biomed. Eng. Lett.* **2024**, *14*, 707−716.

(28) Feng, X. R.; Zhang, Y. Y.; Yang, Z. L.; Zhao, Z. H.; Zhu, F.; Wei, X. Y.; Chen, L. X.; Liu, J. L.; Feng, Y. H.; Li, C. M.; et al. Polyethylene glycol with dual three-dimensional porous carbon nanotube/diamond: a high thermal conductivity of composite PCM. *Nanotechnology* **2024**, *35* (9), No. 095702.

(29) Chawla, K.; Cai, J. Z.; Thompson, D.; Thevamaran, R. Superior thermal transport properties of vertically aligned carbon nanotubes tailored through mesoscale architectures. *Carbon* **2024**, *216*, No. 118526.

(30) Huang, S.; Song, J. L.; Lu, Y.; Lv, C. J.; Zheng, H. X.; Liu, X.; Jin, Z. J.; Zhao, D. Y.; Carmalt, C. J.; Parkin, I. P. Power-free water pump based on a superhydrophobic surface: generation of a mushroom-like jet and anti-gravity long-distance transport. *J. Mater. Chem. A* **2016**, *4* (36), 13771−13777.

(31) Shi, S. L.; Song, J. L.; Zhang, B.; Ma, C.; Jia, P.; Lv, C. J. Capillary drainage of a sessile droplet through a micropore. *Phys. Rev. Fluids* **2020**, *5* (10), No. 104002.

https://doi.org/10.1021/acsnano.4c08108
ACS Nano XXXX, XXX, XXX−XXX

(32) Finn, R. Capillary surface interfaces. *Notices of the AMS* **1999**, *46* (7), 770−781.
(33) Durand, M. Mechanical approach to surface tension and capillary phenomena. *Am. J. Phys.* **2021**, *89* (3), 261−266.
(34) Cheng, X. Q.; Ye, Y. Y.; Li, Z. X.; Chen, X. Y.; Bai, Q.; Wang, K.; Zhang, Y. J.; Drioli, E.; Ma, J. Constructing Environmental-Friendly "Oil-Diode" Janus Membrane for Oil/Water Separation. *ACS Nano* **2022**, *16* (3), 4684−4692.
(35) Degennes, P. G. WETTING - STATICS AND DYNAMICS. *Rev. Mod. Phys.* **1985**, *57* (3), 827−863.
(36) O'Brien, S. B. G. On the shape of small sessile and pendant drops by singular perturbation techniques. *J. Fluid Mech. (UK)* **1991**, *233*, 519−537.
(37) Fatollahi, A. H. On the shape of a lightweight drop on a horizontal plane. *Phys. Scr.* **2012**, *85* (4), No. 045401.
(38) Song, J. L.; Guan, F. S.; Pan, W. H.; Liu, Z. A.; Sun, J.; Ling, S. Y.; Deng, X.; Sun, Y. W. Droplet-Based Self-Propelled Miniboat. *Adv. Funct. Mater.* **2020**, *30* (16), No. 1910778.
(39) Chen, Y.; Yan, D. F.; Liu, R.; Lu, Y.; Zhao, D. Y.; Deng, X.; Song, J. L. Green self-propelling swimmer driven by rain droplets. *Nano Energy* **2022**, *101*, No. 107543.
(40) Dai, R. Y.; Li, G. Q.; Xiao, L.; Li, Y. X.; Cui, Z. H.; Jia, L.; Zhou, M. L.; Song, Y. G.; Yang, Y.; Cai, Y.; et al. A droplet-driven micro-surfboard with dual gradients for programmable motion. *Chem. Eng. J.* **2022**, *446*, No. 136874.

https://doi.org/10.1021/acsnano.4c08108
ACS Nano XXXX, XXX, XXX−XXX